Characterization and control of vortex and antivortex domain defects in quadrilateral ferroelectric nanodots

L. L. Ding,[1,2] Ye Ji,[1,2] X. Y. Zhang,[1,2] W. M. Xiong,[1,2] W. J. Chen,[1,2,3,*] B. M. Zhang,[1,2] Biao Wang,[1,4,†] and Yue Zheng[1,2,‡]

[1]*State Key Laboratory of Optoelectronic Materials and Technologies, School of Physics, Sun Yat-sen University, Guangzhou, 510275, China*

[2]*Micro&Nano Physics and Mechanics Research Laboratory, School of Physics, Sun Yat-sen University, Guangzhou, 510275, China*

[3]*School of Materials, Sun Yat-sen University, Guangzhou, 510275, China*

[4]*Sino-French Institute of Nuclear Engineering and Technology, Sun Yat-sen University, 519082, Zhuhai, China*

(Received 31 March 2019; published 22 October 2019)

Ferroelectric nanostructures have recently attracted considerable research interests for the discovery of novel topological dipole states. However, currently the preparation of high-quality nanodot arrays remains challenging, precluding the clear characterization of the dipole states in the nanodots. Combining pulsed laser deposition method with circular anodic aluminum oxide template, we reported an unexpected growth of high crystalline quality $PbZr_{0.52}Ti_{0.48}O_3$ nanodot array in quadrilateral shape with size being ~80 nm. Piezoresponse force microscopy measurement on various regions of the sample shows that the nanodots form rather diverse in-plane domain patterns, with the appearance of abundant topological domain defects including flux-closure vortices, center-divergent vortices, center-convergent vortices, and antivortices. A deterministic control of the domain structure of the nanodots via applying an electric field is further achieved. The nanodots were found to favor a center-divergent vortex pattern under negative tip bias, although the domain patterns of the nanodots at the as-grown state are different. Phase field simulations were performed to reproduce the experimental observation, and our results indicate that the screening condition of the nanodots is far from the ideal ones assumed in previous theoretical modellings. The nanodots are potentially useful in developing multi-state and reconfigurable electronic devices.

DOI: 10.1103/PhysRevMaterials.3.104417

I. INTRODUCTION

Being an important class of functional materials, ferroelectrics hold promise for potential applications in information processing, sensor and actuator devices for their intriguing properties mediated by ferroelectric polarization and domain structure [1–7]. With the help of state-of-the-art experimental and theoretical techniques, ferroelectric thin film structures (e.g., capacitors and superlattices) have been extensively studied over the past two decades, with the discovery of many important characteristics such as vanishing of ferroelectric critical thickness [8–10], polarization-mediated tunneling electroresistance effects [11–13], abnormal photoelectric effects [14–16], domain wall conductivity [17–19], novel nanoscale topological defects [20–22], etc. In parallel with the research of ferroelectric thin films, low-dimensional ferroelectric nanostructures (LDFNs) like nano-dots, wires and tubes are also attracting much academic interests [23–27], for the even stronger surface and size effects on the ferroelectric polarization and domain structure. However, in contrast with their film counterparts, research on LDFNs is still at the very primary stage due to the challenges in both experimental and theoretical investigations. Academic focuses are currently mainly on revealing the ferroelectric properties such as ferroelectric loops and domain structure in LDFNs [4].

At the early days, LDFNs were believed to possess a rather weak ferroelectricity due to the strong depolarization effect, casting a shadow over the potential application of LDFNs. A milestone work was made in 2003 by Naumov *et al.* [28] who predicted that polarization vortices would form in LDFNs before developing a paraelectric state, with the size of a single polarization vortex as small as several nanometers. Since then, a large number of works have been devoted to the research of this novel topological polarization texture. Notably, theoretical simulations based on effective Hamiltonians, molecular dynamics, phase field models, etc., were performed to reveal the formation conditions and response characteristics of polarization vortices in LDFNs subjected to various external electrical or mechanical stimulus [29–34]. Experimental efforts were also made to identify polarization vortices in LDFNs [35–44]. One can notice the early works where Pb(Zr, Ti)O_3 (PZT) nanodots were prepared by pulsed laser deposition (PLD) method in combination with anodic aluminum oxide (AAO) template [35], and blurry signals of polarization vortex were observed but rarely in some of the nanodots by piezoresponse force microscopy (PFM) [36]. Vortex-like domain patterns (which are actually packets of 90° stripe domains) were found in FIB machined $BaTiO_3$ and PZT platelets based on STEM with a high-angle annular dark field (HAADF) detector [37–39]. More recently, a plenty of exotic

*Authors to whom correspondence should be addressed: chenweijin@mail.sysu.edu.cn

†wangbiao@mail.sysu.edu.cn

‡zhengy35@mail.sysu.edu.cn

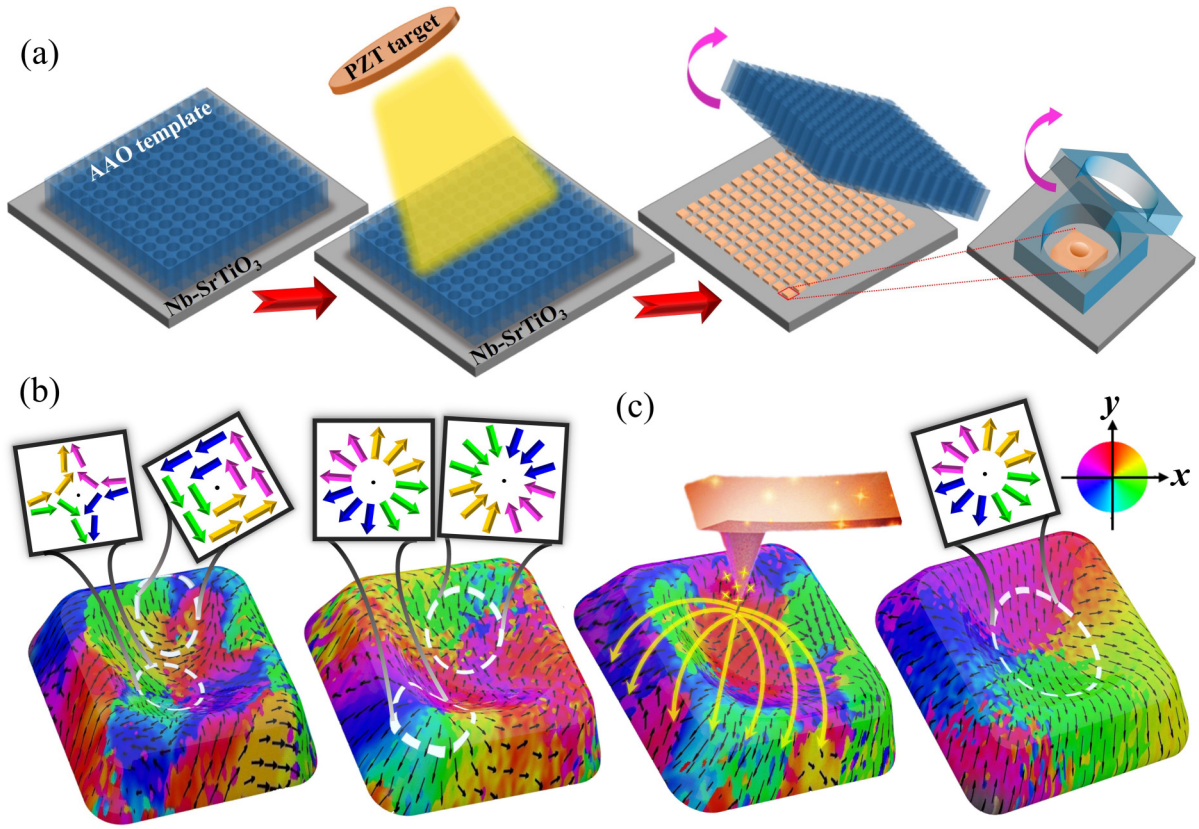

FIG. 1. Schematic illustrations of the preparation process of PZT nanodots and typical topological domain defects observed in the sample. (a) AAO template was transferred onto Nb-$SrTiO_3$ substrate. Then PZT nanodots were deposited by PLD method. After that, AAO template was removed from the substrate to obtain the exposed PZT nanodots. At last, the enlarged view of one deposited nanodot, which are in quadrilateral shape and with a concave center. (b) Schematics of four kinds of vortex and antivortex domain defects in as-grown PZT nanodots. They are flux-closure vortices, center-divergent vortices, center-convergent vortices, and antivortices. (c) Schematic of domain evolution of a nanodot subjected to a tip bias.

and configurable topological textures (such as flux-closure vortices, center-type vortices, and antivortices) were observed by PFM in PLD deposited $BiFeO_3$ nanodots [40–43] with texture-mediated conductance [43]. Three-dimensional (3D) imaging of the vortex structure in a $BaTiO_3$ nanoparticle was also achieved by Bragg diffraction technique and the vortex core was shown to exhibit a reversible transformation path driven by an electric field [44]. Despite of these theoretical and experimental progresses, so far a clear picture on the dipole states of realistic LDFNs is not yet accomplished due to the challenge in preparation of high-quality LDFNs matching the size and surface conditions with those investigated by theoretical works, and also due to the limited spatial resolution and the complicated sample-probe interaction problem of existed polarization characterization techniques. To better understand the dipole states of realistic LDFNs, efforts on growth of high-quality LDFNs and characterization of their dipole states are still greatly demanded.

In this work, with a combination of PLD method and circular AAO template [as schematically shown in Fig. 1(a)], we succeeded in growth of high-crystalline quality $PbZr_{0.52}Ti_{0.48}O_3$ nanodot array, with all the nanodots being quadrilateral shaped and in a lateral size of ~80 nm. To the best of our knowledge, such a large amount of high-quality quadrilateral PZT nanodots has never been achieved by PLD method, and is unexpected as circular AAO template was used. Remarkably, despite the similar size and shape of the nanodots, PFM characterization shows that the as-grown nanodots form rather diverse in-plane domain patterns, with the formation of at least four type vortex and antivortex domain defects including flux-closure vortices, center-divergent vortices, center-convergent vortices, and antivortices [Fig. 1(b)]. What's more, it is found that the nanodots tend to form a similar domain pattern with a center-divergent vortex defect after applying an electric field [Fig. 1(c)]. Our results indicate that the screening condition of the nanodots is far from the ideal ones in previous theoretical modellings, as elaborated by our phase field simulations of nanodot domain structure with taken into account both bulk and surface screening sources. The diverse domain patterns and domain defects of the nanodots and the deterministic control by electric field should be potentially useful in design of multi-state and reconfigurable electronic devices.

II. METHODS

A. Sample preparation

PZT nanodots were deposited on an Nb-doped (001) $SrTiO_3$ substrate by PLD method with the assistance of AAO template. The preparation procedure is illustrated

schematically in Fig. 1(a). AAO template supported by polymethyl methacrylate (PMMA) was first transferred onto a cleansed Nb-doped $SrTiO_3$ substrate. The size of AAO template we chose is ∼105 nm in diameter, ∼250 nm in thickness, and ∼125 nm in pitch of pores. Acetone was used for dissolving the PMMA for about 15 minutes. PZT nanodots were then fabricated on this AAO covered Nb-doped $SrTiO_3$ substrate by PLD method. A KrF excimer laser ($\lambda = 248$ nm) was employed as the pulsed laser source focusing on a rotating PZT target with a laser energy of 300 mJ and a pulse frequency in 5 Hz. The substrate was heated at 600 °C in an oxygen atmosphere of 20 Pa during the deposition progress. After 4000 laser pulse deposition, the sample was then annealed at 650 °C for 10 minutes. Then the sample was cooled down to room temperature. The sample was immersed in 8% NaOH solution for about 40 minutes to remove the AAO template. Finally, there are only PZT nanodots left on the Nb-doped $SrTiO_3$ substrate.

B. Property characterization

The x-ray diffraction (XRD, Smartlab 9kw, Japan) was used as a primary means to probe the phase of substance and crystallinity of the as-grown sample, giving out the fundamental crystal structures and the patterns measured with Cu Kα radiation at a working voltage of 40 kV and a current of 36 mA. The morphology feature of the PZT nanodots were given by scanning electron microscope (SEM, Quanta FEG, U.S.A.). The topographic images, the local piezoresponse loops and the ferroelectric domain structures of the PZT nanodots were measured using atomic force and piezoresponse force microscopy (AFM&PFM, Asylum Research MFP-3D SPM, U.S.A.). A dual-frequency resonance-tracking technique is adopted to improve the PFM sensitivity. To have a better visualization of the domain structure of the nanodots, lateral PFM phase images at two sample orientations with a 90° rotation angle were both measured [45–47] (more details can be found in Fig. S1 [48]). The sample was marked before rotation so that the same scanned area can be tracked. In the field control process, we chose the high voltage holder to ensure that the nanodots are subjected to a large enough voltage variation range. Cr/Pt coated probes (Budget sensors) were used in the AFM and PFM measurements.

C. Phase field simulations

To provide theoretical insights of the domain patterns of PZT nanodots observed in the PFM measurements, phase field simulations were performed in our study. The phase field model captures the evolution of the polarization field in the ferroelectric based on the free energy minimization principle. The polarization evolution obeys the so-called time-dependent Ginsburg Landau (TDGL) equation. Because the evolution of polarization accompanies with change of strain field and electrostatic field, we also incorporate the mechanical and electrostatic equilibrium equations into the modeling. Detailed description of our phase field model can be found elsewhere [31,33,34].

Geometry of the model PZT nanodot system is taken to be similar to that of the as-grown PZT nanodots. According to experimental measurement, the nanodots are in quadrilateral shape with a concave center and size being ∼80 nm. In our modeling, the size of nanodot is taken to be 80 nm × 80 nm × 20 nm. The concave center locates on the top surface of the nanodot with in-plane diameter being 60 nm and with a suitable out-of-plane depth. Pyramid elements were used to discretize the nanodot in such a geometry. The shape function of the element is quadratic Lagrange type and each edge of it is no larger than 2 nm.

The nanodot is assumed to be weakly clamped by the substrate, as the XRD data indicates that there is a large difference of the in-plane lattice parameters between the PZT nanodots (∼4.035 Å) and the $SrTiO_3$ substrate (∼3.905 Å). To mimic such a weak clamping condition, the bottom surface of the simulated nanodot is set to be fixed in displacement and other surfaces are mechanically free. This mechanical condition also guarantees a weakly clamped rhombohedral phase in the nanodot. Screening charges are introduced both internally and externally to induce the formation of otherwise energetically unfavorable domain defects. The degrees of the two screening sources have been carefully tuned to obtain the optimized condition to reproduce the domain patterns in the nanodots observed in experiment. The internal screening originates from the fact that existence of electrons, holes and ionic defects like oxygen vacancies can screen the polarization charges. For simplicity, we lower the depolarization field by a factor of in range of [0, 1] to mimic the internal screening effect. The external screening is caused by the surface charges brought by absorbents in the atmosphere like water. To simulate such an effect, the atmosphere is represented by a surrounding box [34] and a Bardeen type screening layer is assumed to reside at the boundaries of the nanodot. Specifically, in the optimized condition, the internal screening factor set to be 0.8, and the Bardeen screening length is set to be 0.001 nm at the side surfaces and 0.05 nm at the top and bottom surfaces of the nanodot. The combining effects of such an anisotropic surface screening and the internal screening allow the stabilization and evolution behaviors of the nanodot domain pattern similar to those of PFM experiment. The nanodot and surrounding box are connected by the continuity condition of electric displacement. With these settings, the domain pattern of the PZT nanodot at room temperature is simulated by using a few sets of randomly distributed polarization field as initial configurations. More details of the phase field simulation can be found in Fig. S4 to Fig. S8 [48].

III. RESULTS AND DISCUSSION

A. Basic characterization of the PZT nanodots

Figure 2(a) shows the XRD theta-2theta (θ-2θ) scan of the as-grown PZT nanodot sample. The XRD spectra exhibits clear feature peaks at (001) and (002) orientations of $PbZr_{0.52}Ti_{0.48}O_3$ and $SrTiO_3$, which are both in ABO_3 perovskite structure [49]. The rocking curves and reciprocal space maps (RSMs) of our PZT nanodot arrays in (002) and (103) crystal planes are provided in Fig. S2 in Ref. [48]. The full width at half maximum (FWHM) values of the rocking curves at the two peaks are about 0.25 and 0.39, which are even lower than those of the epitaxial PZT films reported in

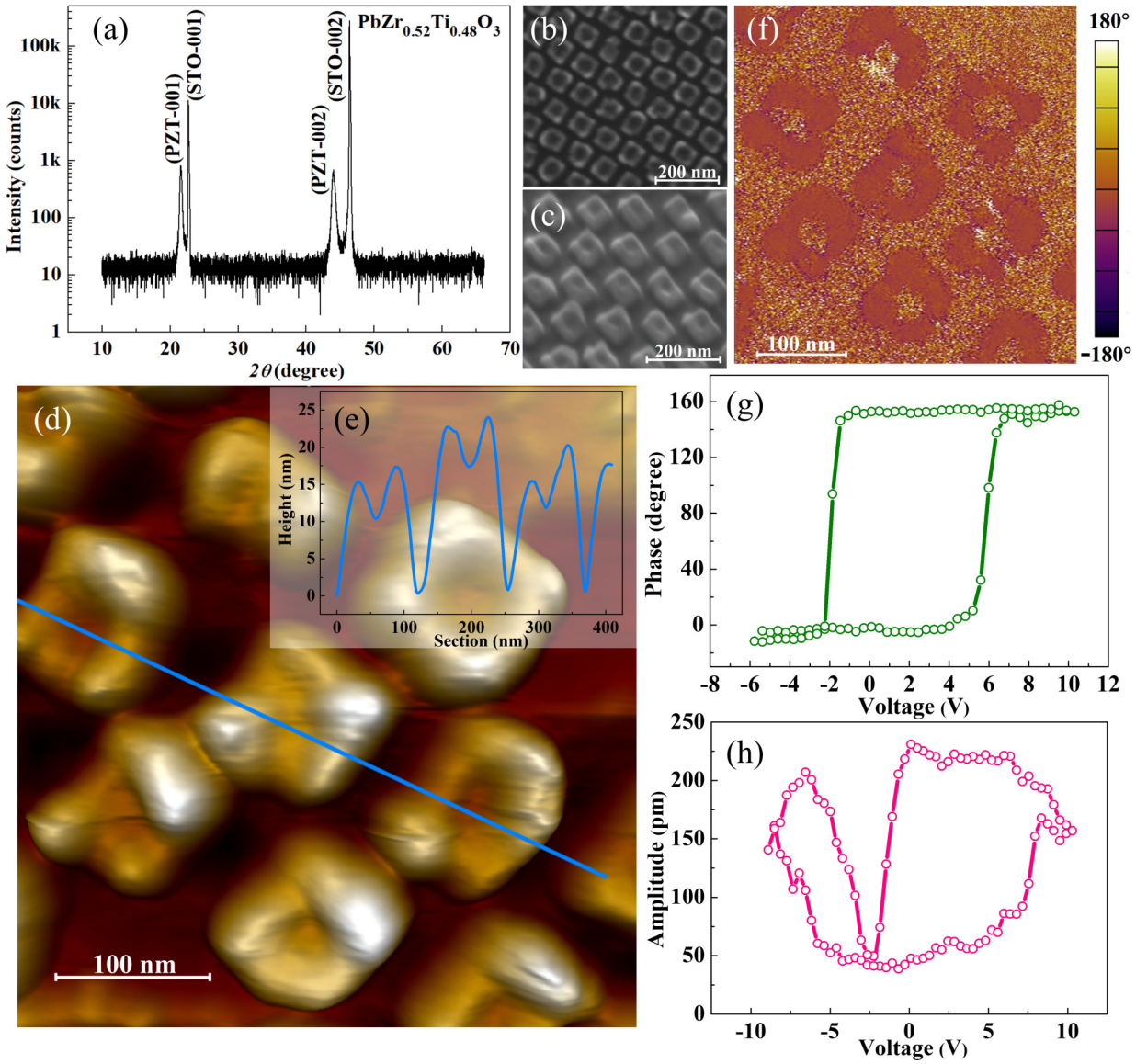

FIG. 2. Basic characterization of the PZT nanodots deposited on an Nb-doped (001) $SrTiO_3$ substrate. (a) XRD diffraction pattern of the nanodot sample. [(b) and (c)] SEM images of the sample at two different angles. (d) 3D AFM morphology images of the nanodots. (e) The height profile of cross-section along the blue line in (d). (f) The out-of-plane phase image measured by PFM. (g) The phase-voltage hysteresis loop and (h) the butterflylike amplitude-voltage loop of a selected nanodot.

previous works [50,51]. Moreover, the RSMs show that the PZT nanodots have a single diffraction peak both in the (002) and (103) reciprocal plane, indicating the high crystalline quality of the PZT nanodots and an epitaxial growth in strain relaxation mode. Based on the relative position of the RSM peaks, one can estimate the lattice parameters of the PZT nanodots to be $a = b \approx 4.035$ Å and $c \approx 4.114$ Å [52,53]. These XRD results together indicate a good epitaxy and crystalline quality of the PZT nanodots.

The good-quality growth of the nanodots is also confirmed from the SEM images [Figs. 2(b) and 2(c)]. It is clear that almost all the nanodots are in a quadrilateral shape, indicating a high degree of crystallinity. The lateral size of the nanodots is around 80 nm, which is smaller than that of the AAO circular pores (which are about 105 nm in diameter). The growth of quadrilateral shaped nanodot array is unexpected as the used AAO template carries circular pores, which should normally help growth of disk or ring shaped structures [54,55]. This indicates that the amount of PZT species entering into the AAO is not enough to fill the pores and the recrystallization process of our nanodot sample is likely to be near an open condition rather than constraint condition, similar to the case of growing square shaped $PbTiO_3$ nanodots by dip-pen lithography [56]. Interestingly, from the SEM images and the 3D AFM morphology images of the nanodots shown in Fig. 2(d), one can clearly see that there is a concave center of each nanodot [a schematic can be found in Fig. 1(a)]. Figure 2(e) depicts the height profile of cross-section along the blue line in Fig. 2(d). The average height and lateral size of the PZT nanodots are determined to be about 20 nm and 80 nm, respectively, and the depth of concave center of the nanodot is about ~5 nm.

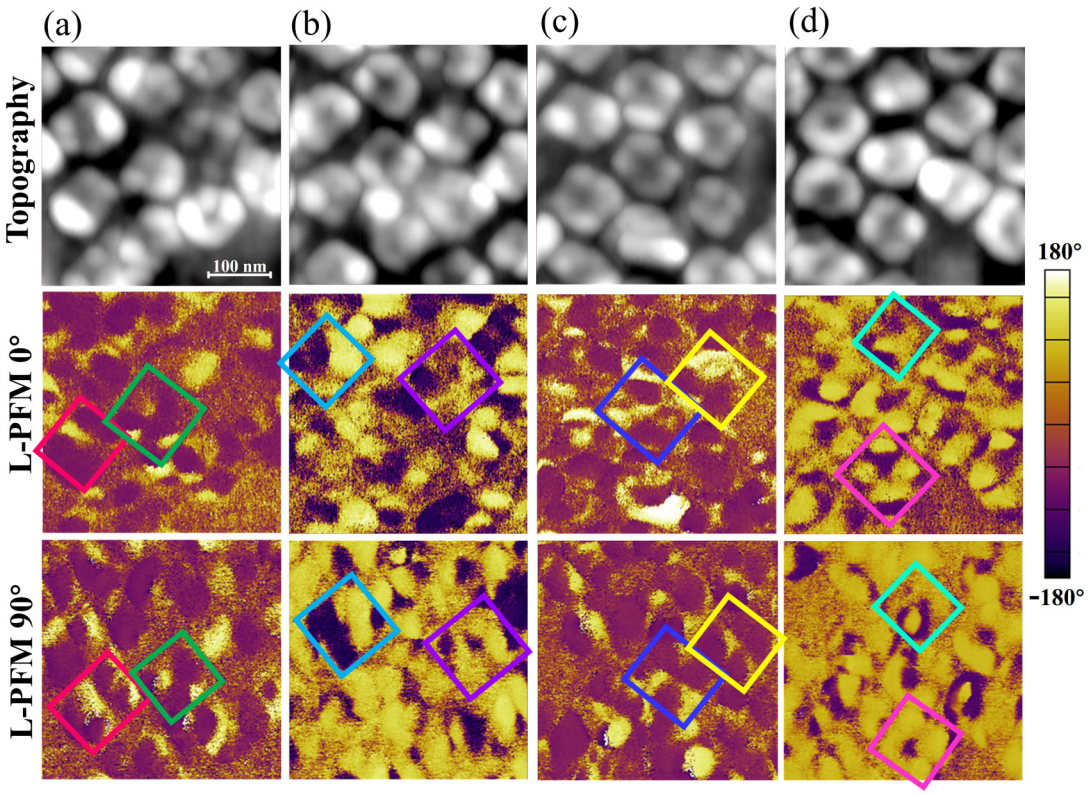

FIG. 3. The topography, lateral PFM phase of 0° (L-PFM 0°) and 90° (L-PFM 90°) at two sample orientations for four selected areas of nanodots (labeled as A, B, C, and D) [(a)–(d)]. For each area, two of the nanodots as labeled with different color squares are picked out for further analysis of the detailed domain pattern and domain defects.

We further measured the local piezoelectric response of the PZT nanodots in the PFM mode. As shown in Fig. 2(f), the out-of-plane piezoelectric phase contrast of the as-grown nanodots is rather weak. Meanwhile, the nanodots show clear phase-voltage hysteresis loop and butterflylike amplitude-voltage loop as shown in Figs. 2(g) and 2(h), indicating a good ferroelectric characteristic of the nanodots. Moreover, PFM image of domain switching in the nanodots after applying bias ±8 V in out-of-plane direction shows a clear out-of-plane phase contrast of the nanodots after domain switching (Fig. S3 in Ref. [48]). The initial weak out-of-plane phase contrast of the as-grown nanodots and the clear out-of-plane phase contrast of the nanodots after domain switching suggest that the nanodots are subjected to a built-in field. Such a built-in field tends to pole the nanodots with an out-of-plane polarization in the same direction, thus the contrast of PFM phase in this direction of the as-grown nanodots is not strong. Note, a built-in field of $\sim 2 \times 10^8$ V/m is also clearly verified by a ∼4 V difference between the positive and negative coercive voltages of the phase-voltage hysteresis loop. The existence of a built-in field may be due to a few possible sources like an asymmetric interfacial condition, the existence of charge defects, as well as the strain-gradient-induced flexoelectric field within the nanodots due to misfit strain relaxation. The origin of built-in field in ferroelectric heterostructures is still in the debate in the literature. One can find many works reporting the observation of built-in fields for the PZT continuous films and other ferroelectric nanostructures, different in magnitudes and even directions [57–60]. Despite of the uncertainty of origin, such a large built-in field tends to pole the out-of-plane polarization of the nanodots in the same direction, and is believed to the reason of the weak out-of-plane PFM phase contrast shown in Fig. 2(f).

B. Domain pattern analysis of the PZT nanodots

To explore the diversity of the domain patterns and possible domain defects of the as-grown PZT nanodots, we performed PFM measurements on the nanodots at four different areas (as labeled by A to D) of the sample. Note, most of the nanodots show weak out-of-plane PFM phase contrasts as those shown in Fig. 2(f), as attributed to the existence of a poling built-in field, whereas the lateral PFM phase exhibits quite diverse patterns [see Figs. 3(a) to 3(d), for area A to D, respectively). Here, lateral PFM phase images at two sample orientations, i.e., L-PFM 0° and L-PFM 90° (which has a 90° rotation of the sample with respect to the L-PFM 0°case), were both measured to provide a better visualization of the in-plane polarization distribution of the nanodots. Remarkably, although the nanodots are in similar shape and size, one can clearly see from Fig. 3 that the nanodots at different areas of the array show rather diverse lateral PFM phase images. Even for nanodots within the same area, they also exhibit quite different lateral PFM phase images with each other, indicating the energy landscape of the nanodots is complicated.

The AFM topography, lateral PFM phase and amplitude images were then used to reconstruct in-plane domain patterns of the nanodots [45–47] (see Ref. [48] for more details of

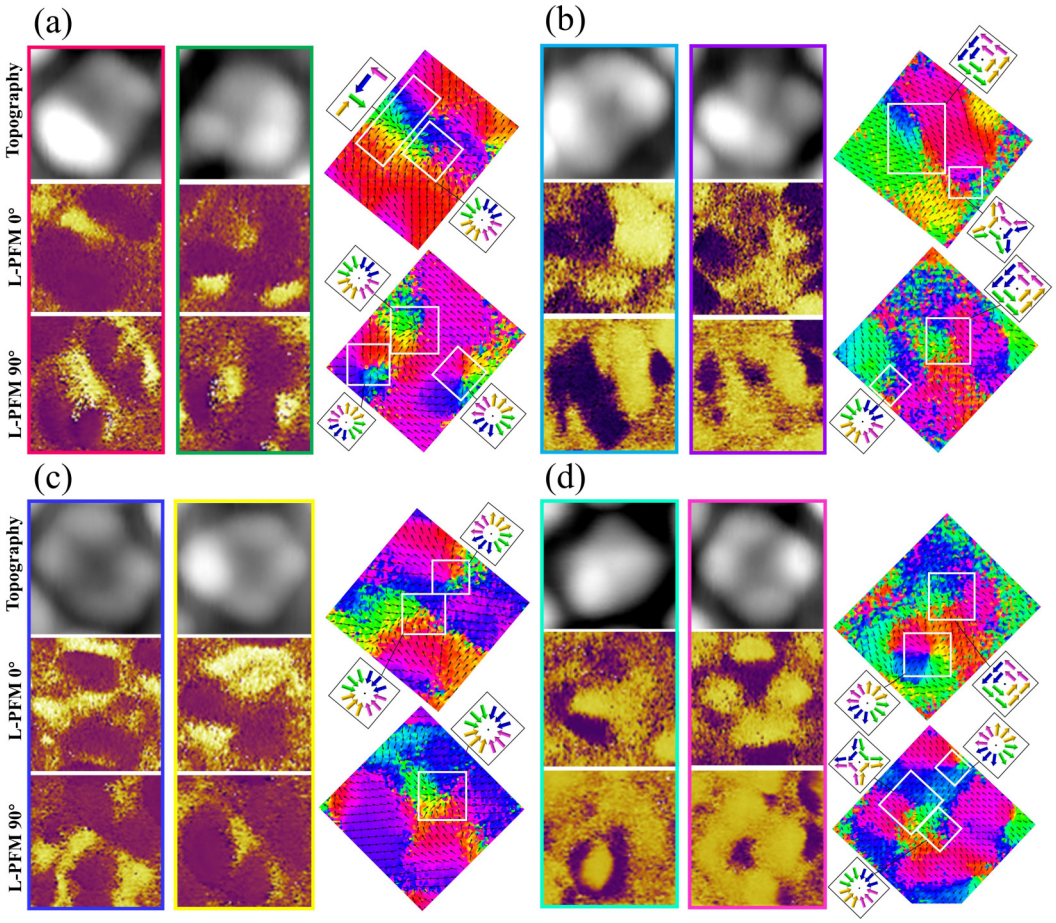

FIG. 4. [(a)–(d)] Analysis of the detailed domain patterns and domain defects of the selected nanodots at areas A to D shown in Fig. 3. Note the selected nanodots are indicated by the color of the PFM image frame which corresponds to the color of the box enclosing the nanodot shown in Fig. 3.

the reconstruction procedure). For each area shown in Fig. 3, two of the nanodots are picked out for analysis of the detailed domain pattern and the domain defects. The constructed domain patterns of the selected nanodots at areas A to D, with the domain defects labeled out, are depicted in Figs. 4(a) to 4(d), respectively. Note, the color of the PFM image frame of the selected nanodots corresponds to the color of the box enclosing the nanodot shown in Fig. 3. From Fig. 4, it is clearly seen that each nanodot contains at least one topological domain defects. One can classify over four kinds of domain defects, including flux-closure vortices, center-divergent vortices, center-convergent vortices, and antivortices. This should be for the first time to report such a diversity of vortex and antivortex domain defects in as-grown PZT nanodots, though similar domain defects have been confirmed in previous works of $BiFeO_3$ nanodots [40–43]. The common forming of such vortex and antivortex domain defects in the nanodots indicates that the screening condition of the nanodots is likely to be at a moderate screening regime (i.e., neither the ideal open-circuited one nor the ideal short-circuited one as commonly assumed in theoretical modellings).

This is elaborated by our phase field simulation which, with taken into account both bulk and surface screening sources, shows that nanodots with moderate bulk and surface screening indeed have the tendency of stabilizing diverse topological domain defects (see Supplementary Materials for more details [48]). Figures 5(a) and 5(b) depict two simulated domain patterns of $Pb(Zr_{0.52}Ti_{0.48})O_3$ nanodots subjected to moderate bulk and surface screening. The two domain patterns were evolved from two different initial random polarization distributions at 300 K in the absence of external electric field. It is clearly seen that the predicted domain defects include flux-closure vortices, center-divergent vortices, center-convergent vortices, and antivortices, similar to those observed in our PFM experiment. It is noteworthy that $PbZr_{0.20}Ti_{0.80}O_3$ nanodots have been grown and found to form regular a/c domain patterns in the nanodots [35]. In the work of Rodriguez *et al.* [36], polarization vortex states were observed in some of the PLD-prepared $PbZr_{0.40}Ti_{0.60}O_3$ nanodots, and the domain patterns in other nanodots seem to be trivial without fruitful domain defects. The rather different domain patterns between the PZT nanodot samples indicates that the PZT composition also has a great effect on the domain pattern of the PZT nanodots. This is like to due to the different ferroelectric phases in these PZT nanodots: $PbZr_{0.20}Ti_{0.80}O_3$ has the simpler tetragonal ferroelectric phase, whereas the ferroelectric phases become more complicated in PZT closer to the morphotropic phase boundary. We believe that the composition of PZT nearby the 52/48 is important for the appearance of fruitful domain defects in our sample. The

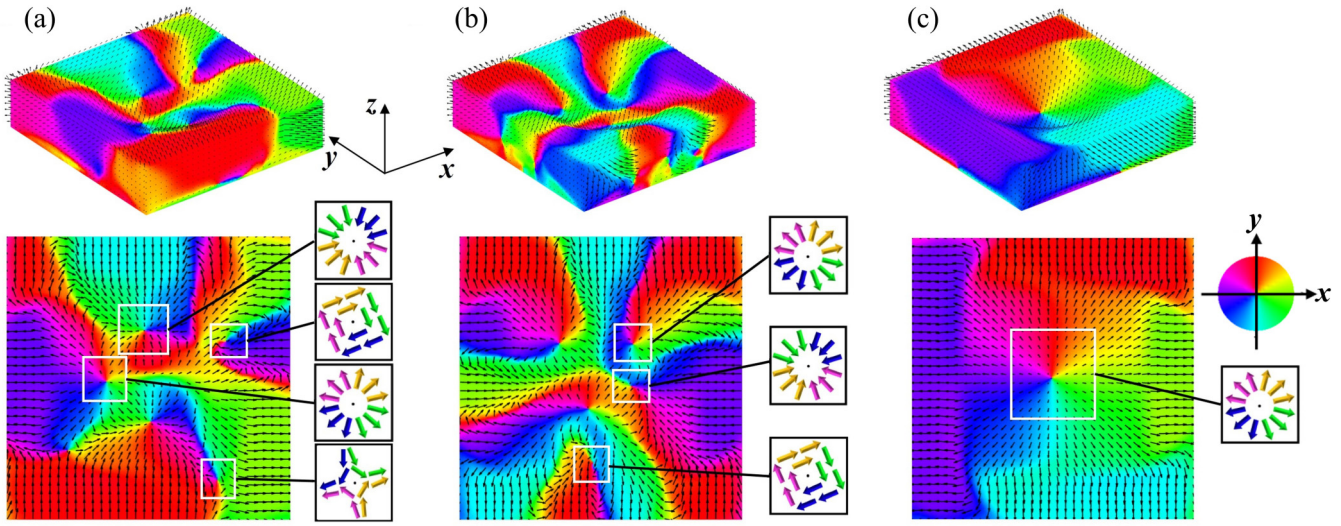

FIG. 5. Phase field simulation results of the domain patterns of PZT nanodots. [(a) and (b)] Two typical domain patterns of PZT nanodots with abundant domain defects at a moderate screening condition in the absence of external electric field. The predicted domain defects are the same as those observed in experiment. (c) The domain pattern of a PZT nanodot after applying the electric field. The nanodot evolves into a domain pattern with only a center-divergent vortex defect.

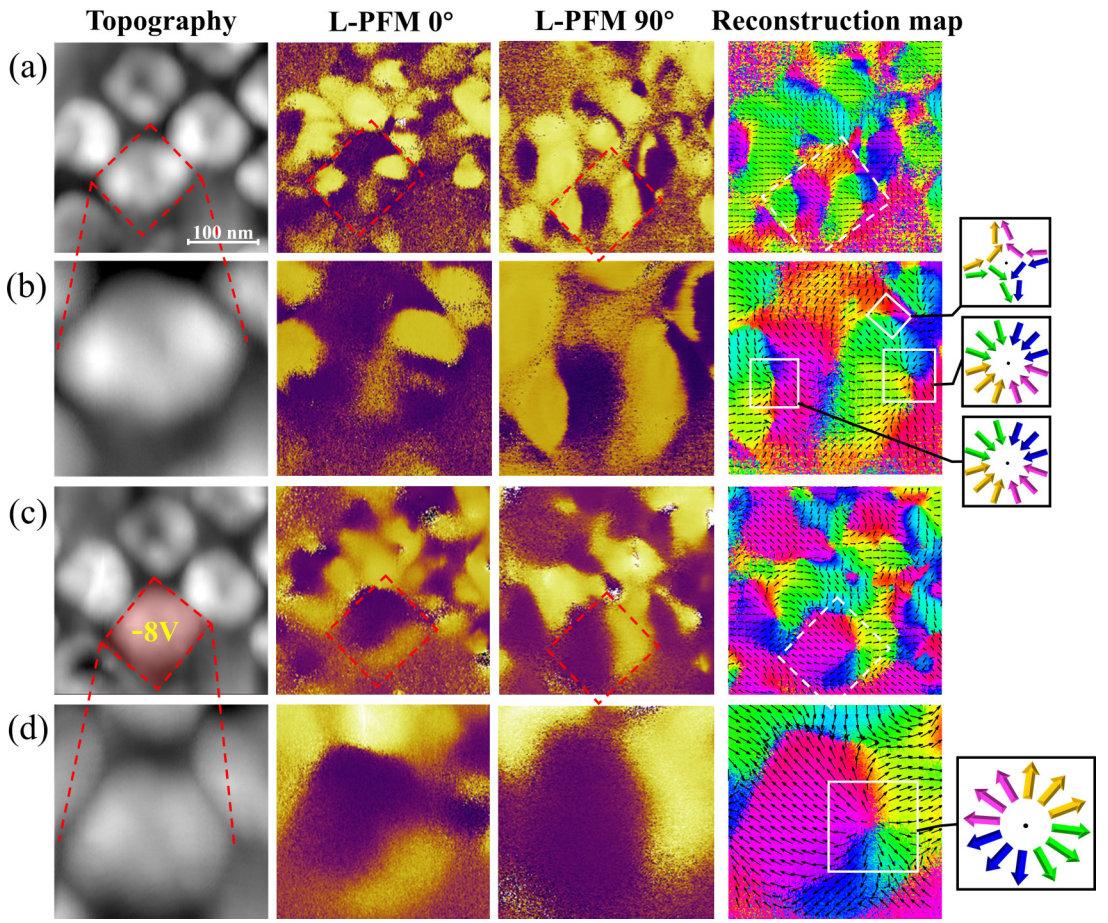

FIG. 6. Evolution of domain pattern under a tip bias of −8 V to a single nanodot (as indicated by the dash boxes in the images). [(a) and (c)] The topography, L-PFM 0°, L-PFM 90° phase images and reconstructed domain patterns before and after applying the tip bias to the nanodot, respectively. [(b) and (d)]. The enlarged view of the topography, L-PFM 0°, L-PFM 90° phase images nearby the nanodot before and after applying the tip bias to the nanodot, respectively.

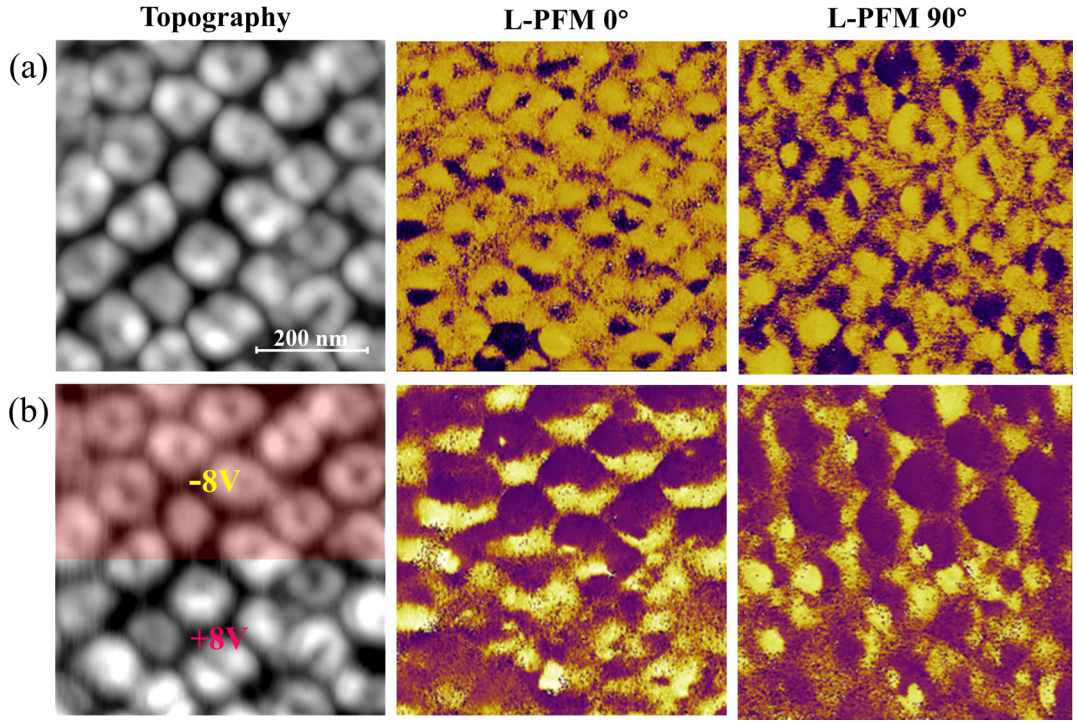

FIG. 7. Evolution of domain pattern of a large area of nanodots under a scanning tip bias of −8 V at the top half region and +8 V at the bottom half region. (a) The topography, L-PFM 0°, L-PFM 90° and phase images before and (b) after applying the tip bias to the nanodot, respectively.

moderate screening and the composition, together with the peculiar size and geometry of the PZT nanodots, lead to a delicate balance between the competitive energies of system, giving rise to fruitful domain patterns and domain defects.

C. Electrical manipulation of the nanodot domain patterns

It is interesting to explore how the diverse domain patterns of PZT nanodots with abundant domain defects evolve under the effect of an electric field. To see this, we applied PFM tip field to the nanodots and compared the domain patterns before and after the field application. Figure 6 depicts the domain pattern evolution of a single nanodot (as indicated by the dash boxes in the PFM images) after applying a tip bias of −8 V. The AFM topography, L-PFM 0°, L-PFM 90° phase images and reconstructed domain patterns before and after applying the tip bias to the nanodot are shown in Figs. 6(a) and 6(c), respectively. To see the domain evolution of the nanodot more clearly, in Figs. 6(b) and 6(d), we also depict the enlarged view of the PFM images of the nanodot. One can clearly see that the domain pattern of the specific nanodot has been changed by the tip bias application, and those of the nearby nanodots have also been affected, indicating a cross-talk effect. The nanodot we concerned forms a domain pattern with a center-divergent vortex, center-convergent vortex, and antivortex before the tip bias application as shown in Fig. 6(b). Interestingly, after the tip bias application, most of the domain defects are erased out, and the nanodot finally evolves into a domain pattern with only a center-divergent vortex defect.

To see the effect of tip bias on the domain pattern of the nanodots more clearly, we further applied a scanning tip bias of −8V to a $600 \times 300\,\mathrm{nm}^2$ region of nanodots. For comparison, we also applied a scanning tip bias of +8V to another $600 \times 300\,\mathrm{nm}^2$ region of nanodots (Fig. 7). The PFM images of the nanodots before and after the tip bias application are shown in Figs. 7(a) and 7(b), respectively. Remarkably, one can see that all the nanodots evolve into a similar pattern with a center-divergent vortex after application of −8 V tip bias, although the initial domain patterns of the nanodots are different. Meanwhile, domain patterns of the nanodots subjected to +8 V positive tip bias change much less significant than those subjected to −8 V positive tip bias. This asymmetric feature is consistent with the existence of a built-in field across the sample as previously discussed in Section III A.

Note, the tendency of forming a domain pattern with a center-divergent vortex of the PZT nanodot under tip bias is also well captured by our phase field simulation. As shown in Fig. 5(c), for the two diverse domain patterns of PZT nanodots obtained at 300 K and at zero field [Figs. 5(a) and 5(b)], after applying an z-directed electric field of $10^9\,\mathrm{V/m}$, these two domain patterns evolve into the same domain pattern with only a center-divergent vortex defect. The evolution into such a simple domain pattern in the PZT nanodots indicates such a domain pattern has a free energy not only lower than those of the as-grown domain patterns with abundant domain defects, but also lower than that of the simple circular vortex domain pattern. In our phase field simulation, a lower energy of the center-divergent domain pattern than the circular vortex domain pattern is guaranteed by the better surface screening at the side surfaces than at the top and bottom surfaces of the nanodot. Otherwise, if the side surfaces of the nanodot are in poor screening, the surface

polarization tends to be parallel to the side surface, and circular vortex domain pattern should be more favored [33]. It is noteworthy that the artificial creation of center-divergent vortex has been recently demonstrated in $BiFeO_3$ films by applying a local tip field via a mechanism different from our systems [61]. The deterministic control of the domain pattern of the PZT nanodots by electric field is potentially useful in developing reconfigurable electronic devices, considering that PZT nanodots also carry texture-sensitive conductance, similar to that demonstrated in $BiFeO_3$ nanodots [43].

IV. CONCLUSION

In summary, PLD method combined with circular AAO template was adopted to grow high crystalline quality PZT nanodot array on an Nb-$SrTiO_3$ substrate. The PZT nanodots exhibit an unexpected quadrilateral shape with a concave center and are in a lateral size of about 80 nm. Interestingly, PFM measurement shows that the as-grown PZT nanodots stabilize rather diverse in-plane domain patterns, with the appearance of abundant domain defects including flux-closure vortices, center-divergent vortices, center-convergent vortices, and antivortices, indicating that the nanodots are subjected to a moderate screening regime different from the ideal ones in previous theoretical modellings. Furthermore, the nanodots were found to show the tendency of forming a center-divergent pattern under negative tip bias, although the domain patterns of the as-grown nanodots are different. The abundant domain patterns and domain defects of the PZT nanodots are potentially useful in developing multistate and reconfigurable electronic devices. The growth of quadrilateral shaped nanodot array with the help of circular AAO template is unexpected. The effects of the growth parameters such as the anneal temperature, the AAO pore size, the pulse number, etc., on the formation of quadrilateral shaped nanodot need to be further explored. It is also an interesting work to further explore the texture-sensitive conductance of the nanodots.

ACKNOWLEDGMENTS

The authors acknowledge support from NSFC (Grants No. 11602310, No. 11672339, and No. 11832019), Guangzhou Science and Technology project (No. 201707020002), and the Fundamental Research Funds for the Central Universities. Y.Z. also acknowledges the support from the Special Program for Applied Research on Super Computation of the NSFC Guangdong Joint Fund (the second phase), the Fok Ying Tung Foundation, the Guangdong Natural Science Funds for Distinguished Young Scholar, and the China Scholarship Council.

[1] M. E. Lines and A. M. Glass, *Principles and Applications of Ferroelectrics and Related Materials* (Oxford University Press, New York, 1979).
[2] P. Muralt, Ferroelectric thin films for micro-sensors and actuators a review, J. Micromech. Microeng. **10**, 136 (2000).
[3] K. M. Rabe, C. H. Ahn, and J. M. Triscone, *Physics of Ferroelectrics: a Modern Perspective* (Springer, Verlag, Berlin, 2007).
[4] J. F. Scott, Applications of modern ferroelectrics, Science **315**, 954 (2007).
[5] R. K. Vasudevan, W. Wu, J. R. Guest, A. P. Baddorf, A. N. Morozovska, E. A. Eliseev, N. Balke, V. Nagarajan, P. Maksymovych, and S. V. Kalinin, Domain wall conduction and polarization-mediated transport in ferroelectrics, Adv. Funct. Mater. **23**, 2592 (2013).
[6] Y. Wang, W. J. Chen, B. Wang, and Y. Zheng, Ultrathin ferroelectric films growth, characterization, physics and applications, Materials **7**, 6377 (2014).
[7] L. W. Martin and A. M. Rappe, Thin-film ferroelectric materials and their applications, Nat. Rev. Mater. **2**, 16087 (2016).
[8] J. Junquera and P. Ghosez, Critical thickness for ferroelectricity in perovskite ultrathin films, Nature (London) **422**, 506 (2003).
[9] G. Gerra, A. K. Tagantsev, and N. Setter, Ferroelectricity in Asymmetric Metal- Ferroelectric-Metal Heterostructures: A Combined First-Principles-Phenomenological Approach, Phys. Rev. Lett. **98**, 207601 (2007).
[10] Y. Zheng, W. J. Chen, X. Luo, B. Wang, and C. H. Woo, Critical properties of nanoscale asymmetric ferroelectric tunnel junctions or capacitors, Acta Mater. **60**, 1857 (2012).
[11] E. Y. Tsymbal and H. Kohlstedt, Tunneling across a Ferroelectric, Science **313**, 181 (2006).
[12] A. Gruverman, D. Wu, H. Lu, Y. Wang, J. W. Jang, and C. M. Folkman, Tunneling electroresistance effect in ferroelectric tunnel junctions at the nanoscale, Nano Lett. **9**, 3539 (2009).
[13] Y. Zheng and C. H. Woo, Giant piezoelectric resistance in ferroelectric tunnel junctions, Nanotechnology **20**, 075401 (2009).
[14] S. Y. Yang, J. Seidel, S. J. Byrnes, P. Shafer, C. H. Yang, M. D. Rossell, P. Yu, Y.-H. Chu, J. F. Scott, J. W. Ager, III, L. W. Martin, and R. Ramesh, Above-bandgap voltages from ferroelectric photovoltaic devices, Nat. Nanotech. **5**, 143 (2010).
[15] K. Chu, B.-K. Jang, J. H. Sung *et al.*, Enhancement of the anisotropic photocurrent in ferroelectric oxides by strain gradients, Nat. Nanotech. **10**, 972 (2015).
[16] M. M. Yang, D. J. Kim, and M. Alexe, Flexo-photovoltaic effect, Science **360**, 904 (2018).
[17] E. A. Eliseev, A. N. Morozovska, G. S. Svechnikov, V. Gopalan, and V. Ya. Shur, Static conductivity of charged domain walls in uniaxial ferroelectric semiconductors, Phys. Rev. B **83**, 235313 (2011).
[18] D. Meier, J. Seidel, A. Cano, K. Delaney, Y. Kumagai, M. Mostovoy, N. A. Spaldin, R. Ramesh, and M. Fiebig, Anisotropic conductance at improper ferroelectric domain walls, Nat. Mater. **11**, 284 (2012).
[19] A. Crassous, T. Sluka, A. K. Tagantsev, K. Delaney, Y. Kumagai, M. Mostovoy, N. A. Spaldin, R. Ramesh, and M. Fiebig, Polarization charge as a reconfigurable quasi-dopant in ferroelectric thin films, Nat. Nanotech. **10**, 614 (2015).
[20] Y. Nahas, S. Prokhorenko, L. Louis, Z. Gui, I. Kornev, and L. Bellaiche, Discovery of stable skyrmionic state in ferroelectric nanocomposites, Nat. Commun. **6**, 8542 (2015).

[21] L. Lu, Y. Nahas, M. Liu, H. C. Du, Z. Jiang, S. Ren, D. Wang, L. Jin, S. Prokhorenko, C.-L. Jia, and L. Bellaiche, Topological Defects with Distinct Dipole Configurations in $PbTiO_3/SrTiO_3$ Multilayer Films, Phys. Rev. Lett. **120**, 177601 (2018).

[22] Q. Zhang, S. Prokhorenko, Y. Nahas, L. Xie, L. Bellaiche, A. Gruverman, and N. Valanoor, Deterministic switching of ferroelectric bubble nanodomains, Adv. Funct. Mater. **29**, 1808573 (2019).

[23] J. Kim, S. A Yang, Y. C. Choi, J. K. Han, K. O. Jeong, Y. J. Yun, D. J. Kim, S. M. Yang, D. Yoon, H. Cheong, K.-S. Chang, T. W. Noh, and S. D. Bu, Ferroelectricity in highly ordered arrays of ultra-thin-walled Pb(Zr, Ti)O_3 nanotubes composed of nanometer-sized perovskite crystallites, Nano Lett. **8**, 1813 (2008).

[24] W. S. Yun, J. J. Urban, Q. Gu, and H. Park, ferroelectric properties of individual barium titanate nanowires investigated by scanned probe microscopy, Nano Lett. **2**, 447 (2002).

[25] A. N. Morozovska, E. A. Eliseev, and M. D. Glinchuk, Ferroelectricity enhancement in confined nanorods: Direct variational method, Phys. Rev. B **73**, 214106 (2006).

[26] Y. Zheng, C. H. Woo, and B. Wang, Surface tension and size effect in ferroelectric nanotubes, J. Phys.: Condens. Matter **20**, 135216 (2008).

[27] P. M. Rørvik, T. Grande, and M.-A. Einarsrud, One-dimensional nanostructures of ferroelectric perovskites, Adv. Mater. **23**, 4007 (2011).

[28] I. I. Naumov, L. Bellaiche, and H. Fu, Unusual phase transitions in ferroelectric nanodisks and nanorods, Nature **432**, 737 (2004).

[29] I. Naumov and H. Fu, Vortex-to-Polarization Phase Transformation Path in Ferroelectric Pb(ZrTi)O_3 Nanoparticles, Phys. Rev. Lett. **98**, 077603 (2007).

[30] M. G. Stachiotti and M. Sepliarsky, Toroidal Ferroelectricity in $PbTiO_3$ Nanoparticles, Phys. Rev. Lett. **106**, 137601 (2011).

[31] W. J. Chen and Y. Zheng, Vortex switching in ferroelectric nanodots and its feasibility by a homogenous electric field, Acta Mater. **88**, 41 (2015).

[32] L. V. Lich, T. Shimada, J. Wang, V.-H. Dinh, T. Q. Bui, and T. Kitamura, Switching the chirality of a ferroelectric vortex in designed nanostructures by a homogeneous electric field, Phys. Rev. B **96**, 134119 (2017).

[33] Y. Zheng and W. J. Chen, Characteristics and controllability of vortices in ferromagnetics, ferroelectrics, and multiferroics, Rep. Prog. Phys. **80**, 086501 (2017).

[34] Y. Ji, W. J. Chen, and Y. Zheng, Crossover of polar and toroidal orders in ferroelectric nanodots with a MPB and nonvolatile polar-vortex transformations, Phys. Rev. B **100**, 014101 (2019).

[35] W. Lee, H. Han, A. Lotnyk, M. A. Schubert, S. Senz, M. Alexe, D. Hesse, S. Baik, and U. Gosele, Individually addressable epitaxial ferroelectric nanocapacitor arrays with near Tb $inch^{-2}$ density, Nat. Nanotech. **3**, 402 (2008).

[36] B. J. Rodriguez, X. S. Gao, L. F. Liu, W. Lee, I. I. Naumov, A. M. Bratkovsky, D. Hesse, and M. Alexe, Vortex polarization states in nanoscale ferroelectric arrays, Nano Lett. **9**, 1127 (2009).

[37] L. J. McGilly and J. M. Gregg, Polarization closure in $PbZr_{(0.42)}Ti_{(0.58)}O_3$ nanodots, Nano Lett. **11**, 4490 (2011).

[38] A. Schilling, S. Prosandeev, R. G. P. McQuaid, L. Bellaiche, J. F. Scott, and J. M. Gregg, Shape-induced phase transition of domain patterns in ferroelectric platelets, Phys. Rev. B **84**, 064110 (2011).

[39] R. Ahluwalia, N. Ng, A. Schilling, R. G. P. McQuaid, D. M. Evans, J. M. Gregg, D. J. Srolovitz, and J. F. Scott, Manipulating Ferroelectric Domains in Nanostructures Under Electron Beams, Phys. Rev. Lett. **111**, 165702 (2013).

[40] Z. Li, Y. Wang, G. Tian, P. Li, L. Zhao, F. Zhang, J. Yao, H. Fan, X. Song, D. Chen, Z. Fan, M. Qin, M. Zeng, Z. Zhang, X. Lu, S. Hu, C. Lei, Q. Zhu, J. Y. Li, X. S. Gao, and J. M. Liu, High-density array of ferroelectric nanodots with robust and reversibly switchable topological domain states, Sci. Adv. **3**, e1700919 (2017).

[41] G. Tian, D. Chen, H. Fan, P. Li, Z. Fan, M. Qin, M. Zeng, J. Dai, X. S. Gao, and J.-M. Liu, Observation of exotic domain structures in ferroelectric nanodot arrays fabricated via a universal nanopatterning approach, ACS Appl. Mater. Interfaces **9**, 37219 (2017).

[42] K.-E. Kim, S. Jeong, K. Chu, J. H. Lee, G.-Y. Kim, F. Xue, T. Y. Koo, L.-Q. Chen, S.-Y. Choi, R. Ramesh, and C.-H. Yang, Configurable topological textures in strain graded ferroelectric nanoplates, Nat. Commun. **9**, 403 (2018).

[43] J. Ma, J. Ma, Q. Zhang, R. Peng, J. Wang, C. Liu, M. Wang, N. Li, M. Chen, X. Cheng, P. Gao, L. Gu, L.-Q. Chen, P. Yu, J. X. Zhang, and C.-W. Nan, Controllable conductive readout in selfassembled, topologically confined ferroelectric domain walls, Nat. Nanotech. **13**, 947 (2018).

[44] D. Karpov, Z. Liu, T. dos Santos Rolo, R. Harder, P. V. Balachandran, D. Xue, T. Lookman, and E. Fohtung, Three-dimensional imaging of vortex structure in a ferroelectric nanoparticle driven by an electric field, Nat. Commun. **8**, 280 (2017).

[45] S. V. Kalinin, B. J. Rodriguez, S. Jesse, J. Shin, A. P. Baddorf, P. Gupta, H. Jain, D. B. Williams, and A. Gruverman, Vector piezoresponse force microscopy, Microsc. Microanal. **12**, 206 (2006).

[46] J. T. Heron, J. L. Bosse, Q. He, Y. Gao, M. Trassin, L. Ye, J. D. Clarkson, C. Wang, Jian Liu, S. Salahuddin, D. C. Ralph, D. G. Schlom, J. Iniguez, B. D. Huey, and R. Ramesh, Deterministic switching of ferromagnetism at room temperature using an electric field, Nature (London) **516**, 370 (2014).

[47] D. A. Bonnell, S. V. Kalinin, A. L. Kholkin, and A. Gruverman, Piezoresponse force microscopy: A window into electromechanical behavior at the nanoscale, MRS Bull. **34**, 648 (2009).

[48] See Supplemental Material at http://link.aps.org/supplemental/10.1103/PhysRevMaterials.3.104417 for additional experimental and simulation details and results.

[49] J. N. Wang, L. D. Wang, W. L. Li, and W. D. Fei, Dependence of lattice distortion of monoclinic phase on film thickness in $Pb(Zr_{0.58}Ti_{0.42})O_3$ thin films, J. Alloys Compd. **509**, 3347 (2011).

[50] M. D. Nguyen, C. T. Q. Nguyen, H. N. Vu, and G. Rijnders, Experimental evidence of breakdown strength and its effect on energy storage performance in normal and relaxor ferroelectric films, Curr. Appl Phys. **19**, 1040 (2019).

[51] M.-F. Tsai, J. Jiang, P.-W. Shao, Y.-H. Lai, J.-W. Chen, S.-Z. Ho, Y.-C. Chen, D.-P. Tsai, and Y.-H. Chu Oxide heteroepitaxy-based flexible ferroelectric transistor, ACS Appl. Mater. Interfaces **11**, 25882 (2019).

[52] M. Botea *et al.*, Structural, electric and pyroelectric properties of up and down graded PZT multilayers, Curr. Appl Phys. **19**, 804 (2019).

[53] S. Yin *et al.*, Epitaxial growth and electrical measurement of single crystalline $Pb(Zr_{0.52}Ti_{0.48})O_3$ thin film on Si (001) for micro-electromechanical systems, Thin Solid Films **520**, 4572 (2012).

[54] Q. Luo, D. Chen, W. Yang, C. Chen, P. Li, Z. Huang, G. Tian, Z. Fan, X. S. Gao, and J.-M. Liu, Fabrication of epitaxial ferroelectric $BiFeO_3$ nanoring structures by a two-step nanopatterning method, Ceram. Int. **43**, 16136 (2017).

[55] G. Tian, D. Chen, J. Yao, Q. Luo, Z. Fan, M. Zeng, Z. Zhang, J. Dai, X. S. Gao, and J.-M. Liu, $BiFeO_3$ nanorings synthesized via AAO template-assisted pulsed laser deposition and ion beam etching, RSC Adv. **7**, 41210 (2017).

[56] J. Y. Son, Y. H. Shin, S. Ryu, H. Kim, and H. M. Jang, Dippen lithography of ferroelectric $PbTiO_3$ nanodots, J. Am. Chem. Soc. **131**, 14676 (2009).

[57] W. Wu, K. H. Wong, and C. L. Choy, Interface-oxygen-loss-controlled voltage offsets in epitaxial $Pb(Zr_{0.52}Ti_{0.48})O_3$ thin-film capacitors with $La_{0.7}Sr_{0.3}MnO_3$ electrodes, Appl. Phys. Lett. **85**, 5013 (2004).

[58] W. Wu, Y. Wang, G. K. H. Pang, K. H. Wong, and C. L. Choy, Effect of lattice-misfit strain on the process-induced imprint behavior in epitaxial $Pb(Zr_{0.52}Ti_{0.48})O_3$ thin films, Appl. Phys. Lett. **85**, 1583 (2004).

[59] W. H. Ma and H. Dietrich, Polarization imprint in ordered arrays of epitaxial ferroelectric nanostructures, Appl. Phys. Lett. **84**, 2871 (2004).

[60] H. Lee, T. H. Kim, J. J. Patzner *et al.* Imprint control of $BaTiO_3$ thin films via chemically induced surface polarization pinning, Nano Lett. **16**, 2400 (2016).

[61] J. Kim, M. You, K.-E. Kim, K. Chu, and C.-H. Yang, Artificial creation and separation of a single vortex–antivortex pair in a ferroelectric flatland, npj Quantum Mater. **4**, 29 (2019).